Droplet retention time and pressure drop in SiSiC open-cell foams used as droplet separation devices – A numerical approach

Hernandez, J. N. C.; Lecrivain, G.; Schubert, M.; Hampel, U.;

Originally published:

September 2020

Industrial & Engineering Chemistry Research 59(2020)9, 4093-4107

DOI: https://doi.org/10.1021/acs.iecr.9b04247

Thermodynamics, Transport, and Fluid Mechanics

Droplet retention time and pressure drop in SiSiC open-cell foams used as droplet separation device – A numerical approach

Jesus Nain Camacho Hernandez, Gregory Lecrivain, Markus Schubert, and Uwe Hampel

Ind. Eng. Chem. Res., **Just Accepted Manuscript** • DOI: 10.1021/acs.iecr.9b04247 • Publication Date (Web): 25 Sep 2019

Droplet retention time and pressure drop in SiSiC open-cell foams used as droplet separation device – A numerical approach

Jesus Nain Camacho Hernandez,[a] *Gregory Lecrivain,*[a] *Markus Schubert,*,*[a] *Uwe Hampel*[a,b]

[a] Helmholtz-Zentrum Dresden-Rossendorf, Institute of Fluid Dynamics, Bautzner Landstr. 400, 01328 Dresden, Germany

[b] Technische Universität Dresden, Chair of Imaging Techniques in Energy and Process Engineering, 01062 Dresden, Germany

* Corresponding author: *Tel: +49 351 260 2627, E-mail: m.schubert@hzdr.de*

Abstract

Open-cell foams are a promising alternative for the separation of liquid droplets suspended in gas flows at comparably low pressure drop. The separation in such ceramic foams is investigated using the residence time distribution of droplets derived from pore-scale CFD-simulations. 20 and 45 pores per inch (ppi) silicon-infiltrated silicon carbide (SiSiC) open-cell foams samples are considered. The foam structure was reconstructed from micro-computed tomography (μCT) images. To track the droplets, a Lagrangian discrete-phase model was used. The effect of pore size and pore density on the droplet retention time was studied. The flow pressure drop showed a remarkable agreement with the in-house experimental measurements. The droplet separation efficiency within the foam structure was found to generally increase with the inlet gas velocity and the droplet inertia.

Keywords: Ceramic foams, liquid droplet entrainment, gas-droplet flow, resolved pore-scale CFD simulations, droplet residence time, droplet separator device.

1 Introduction

1.1 Open-cell foams for droplet entrainment

Many industrial systems are adversely affected by the entrainment of liquid droplets in gas flows. In aero-engines, the entrainment of oil lubrication droplets is responsible for both a decrease in performance of fuel engines and an increase in oil consumption.[1] In gas turbines, droplets entrained in the low-pressure part can damage the blades.[2] In bubble column reactors,

reactions can take place in undesirable places as a consequence of droplet entrainment. Chemical reaction may occur in the downstream units.[3] In healthcare facilities, the risk of virus propagation is significantly increased by liquid droplets entrained by air ventilation systems.[4]

Porous materials, such as the open-cell foam illustrated in Figure 1, can be used to mitigate droplets propagation. Such materials allow gases to easily pass through the porous structure, while providing an enhanced separation efficiency caused by a high probability of droplet collision within the foam structure. This is attributed to the large specific surface area of the foam.

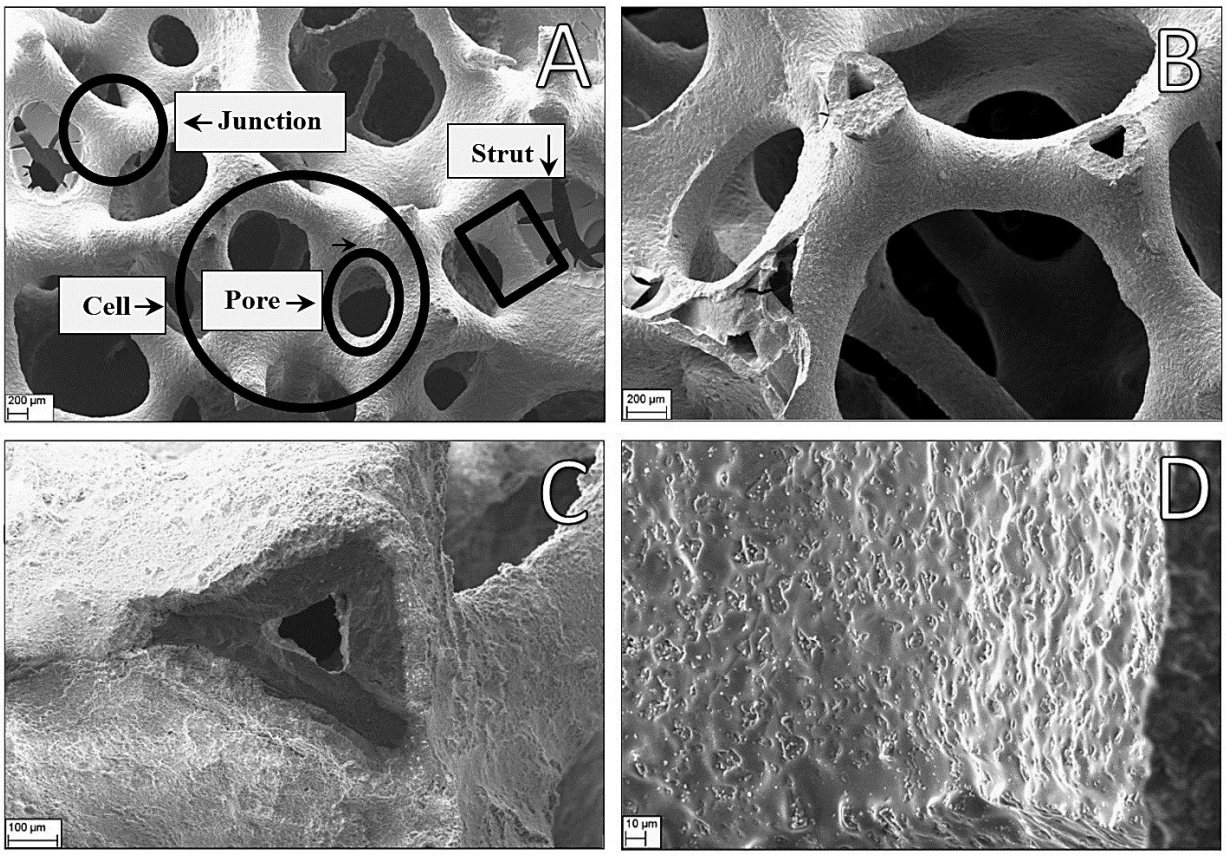

Figure 1: Scanning electron microscopy of a 20 ppi SiSiC foam (image A) showing the structure

of the open-cells. Images (B) and (C) show the empty structure of the struts (isolated from the pore flow). Image (D) shows that the surface is closed.

Research on open-cell porous foams as droplet separators has so far been scarcely addressed. The permeability, which indicates how easily a fluid can pass through a porous media, is a frequently used design parameter. However, the permeability does not provide sufficient information on the porous foam geometry, which plays an important role in the droplet impact with the skeletal network, and in turn, in the droplet residence time. The vast majority of the flow simulations in foams used simple equivalent geometries, such as spheres or cylinders, to represent the porous structure.[5,6] Numerical flow studies in resolved porous structures can provide much more detailed information.

In this work, droplet separation in open-cell ceramic foams is studied using droplet retention times and droplet separation efficiencies computed from CFD simulations. Among the vast list of open-cell foams, silicon-infiltrated silicon carbide foam, (SiSiC - constituted of a silicon carbide matrix and infiltrated free silicon) was presently used due to its promising properties.[7] It has a solid skeleton and exhibits high heat conduction, good thermal shock resistance and low pressure drop.

1.2 Pressure drop models

The hydrodynamics of the gas flow in open-cell foams are of high importance. In particular, the pressure drop plays a crucial role. Several models and correlations have been developed to relate the pressure drop (Δp) to the foam porosity (ε). The porosity is defined as the ratio of the volume

of voids to the total volume of the material. One of the first models was proposed by Darcy (1856) and is now often referred to as the "Darcy equation". This empirical equation relates the pressure drop to the volumetric flow velocity (v_f) normal to the cross-sectional area of the flow, the fluid viscosity (μ_L) and the Darcy's permeability (K) according to

$$v_f = \frac{K}{\mu_L}\Delta p \,. \tag{1}$$

Darcy´s law lacks an inertial term and is therefore only valid at low Reynolds number (Re≪1). At higher Reynolds number, the inertial effect increases quadratically with the fluid velocity. For this reason, a second term representing the kinetic energy of the inertial flow yields the improved Darcy-Forchheimer equation

$$\Delta p = v_f \frac{\mu_L}{K} + C\rho_L |v_f| v_f \,. \tag{2}$$

Both the permeability (K) and the Forchheimer coefficient (C) must be experimentally determined. For a porous packed bed of spheres, Ergun (1952) suggested a dependency of the Fochheimer coefficient and the Darcy-permeability as

$$C = \frac{\beta}{K(1-\varepsilon)} \frac{d_p}{} \text{ and } \frac{1}{K} = \alpha \frac{(1-\varepsilon)^2}{\varepsilon^3 d_p^2} \,. \tag{3}$$

Applying α = 150 and β = 1.75 leads to the well-known Ergun equation

$$\Delta p = 150\frac{(1-\varepsilon)^2\mu_L}{\varepsilon^3 d_p^2}v_f + 1.75\frac{(1-\varepsilon)\rho_L}{\varepsilon^3 d_p}|v_f|v_f\,. \quad (4)$$

Many correlations for the overall pressure drop in open-cell foams can be found in the literature.[5] In most of these correlations, the Ergun's model is associated with a specific porous property, such as the equivalent pore diameter of either a sphere or a cylinder. Two correlations are here of particular importance.

The Lacroix correlation[8] is based on a cubic cell model and relates the diameter of the strut (i.e. cylindrical filaments that envelop a cubic cellular structure) to a strut diameter. In that correlation, where the strut diameter is replaced with the "equivalent particle" diameter (d_d) of an equivalent sphere, the pressure drop is given by

$$\Delta p = \frac{600(1-\varepsilon)^2\mu_L}{9\varepsilon^3 d_s^2}v_f + \frac{7(1-\varepsilon)\rho_L}{6\varepsilon^3 d_s}|v_f|v_f \qquad \text{with} \qquad d_s = \frac{4}{6}d_d\,. \quad (5)$$

The Du Plessis correlation[9] also uses a cubic cell model. A numerical analysis of the three-dimensional steady flow through a series of samples were performed to obtain an empirical expression that relates the porosity to an empirical coefficient (X) as

$$\Delta p = \frac{36X(X-1)(3-X)^2\mu_L}{4\varepsilon^2 a^2}v_f + \frac{2.05X(X-1)\rho_L}{2\varepsilon^2 a}|v_f|v_f\,, \quad (6)$$

where

$$X = 2 + 2cos\left(\frac{4\pi}{3} + \frac{1}{3}cos^{-1}(2\varepsilon - 1)\right). \quad (7)$$

While the pressure drop can be predicted using fairly accurate semi-empirical correlations, there exist no correlations to predict both the ratio of droplets separated from gas flow by open-cell ceramic foams and the residence time of droplets within foams. Such information can either be obtained from experimental work or from Computational Fluid Dynamics (CFD)

1.3 Residence time distributions computed by 3D CFD simulations

CFD simulations in intricate 3D geometries are normally difficult to set up. Hence, equivalent geometric models based on simple geometries (e.g. spheres or cylinders) are often preferred. More realistic reconstructed geometries can be gained from tomographic data, for instance from computed tomography or magnetic resonance imaging. X-ray microtomography is a non-destructive scanning technology that allows obtaining a precise representation of the skeletal structure of foams. The high accuracy with a space resolution down to 20 μm[10] of the obtained 3D volume allows realistic CFD flow simulations.

A practical concept used in engineering is that of the residence time. Roughly speaking, the residence time describes how much time a droplet has spent in a section of a volume regardless of the main flow features (dead spaces, circulation, flow profile, etc.). The time distribution of the various arriving droplets is called the residence time distribution (RTD). Global RTDs can be obtained by adding droplets as tracers to the flow and measuring the number that cross inlet and exit of a volume.[11] Typically, the RTD is represented by either a residence time distribution

function or a histogram, which is the response to an infinitely short (Dirac) impulse and includes the information on the "mean time" spent by the droplet in a continuous system and its variance. In addition to experimental tracer measurements, RTD can also be determined from detailed spatial flow field distributions obtained using CFD simulations. For example, Zou et al.[12] and Kalaga[13] determined the solid residence time distribution in multi-compartment and multistage fluidized beds, respectively, and Cruz-Díaz et al.[14] compared experimental and simulated residence time distribution curves from a filter-press electrochemical reactor. Generally, good agreement between RTD curves obtained using CFD and experimentally was achieved.

2 Methods: Image analysis and process

2.1 Images acquisition

For a visual examination of the structure of SiSiC foams, samples with two different nominal pore dimensions, 20 ppi and 45 ppi (manufactured by IKTS Fraunhofer, Germany), were analyzed with a scanning electron microscope (SEM). An exemplary series of images is shown in Figure 1. The open-foam structure features a convex triangular strut shape (Figure 1**Figure 1**B, 1C). A closer zoom reveals some crystal structures attached to the surface (Figure 1D). Cavities in the interior of struts are practically isolated from the main flow and thus, can be assumed insignificant for the external flow through the pores. Therefore, the flow is only considered in the pore domain and the cavities are withdrawn from CFD models, which in-turn reduces the complexity and the computational cost.

A series of 2D digital cross-sectional images of the 20 ppi and the 45 ppi foam samples (40 mm × 40 mm × 25 mm) with a resolution of 56 x 56 μm^2 per pixel were obtained by IKTS (Germany) X-ray micro-computed tomography (μCT). The 3D image reconstruction from the raw attenuation tomographic datasets was carried out using the filtered back-projection algorithm.

2.2 Image processing

The images illustrated in Figure 2A present undesirable defects and aberrations, such as double edges, streaking, and noise caused by X-ray scattering and beam hardening. Therefore, image post-processing had to be performed through contrast adjustment, edge sharpening, 2D median filtering and segmentation (see Figure 2B). Subsequently, the particle analysis algorithm implemented in the ImageJ[15] software package was used to generate images composed only of strut cavities, which were afterwards subtracted from the original images to obtain cross-sectional images without strut cavities (see Figure 2C). The resulting 3D representation is shown in Figure 2D (far right).

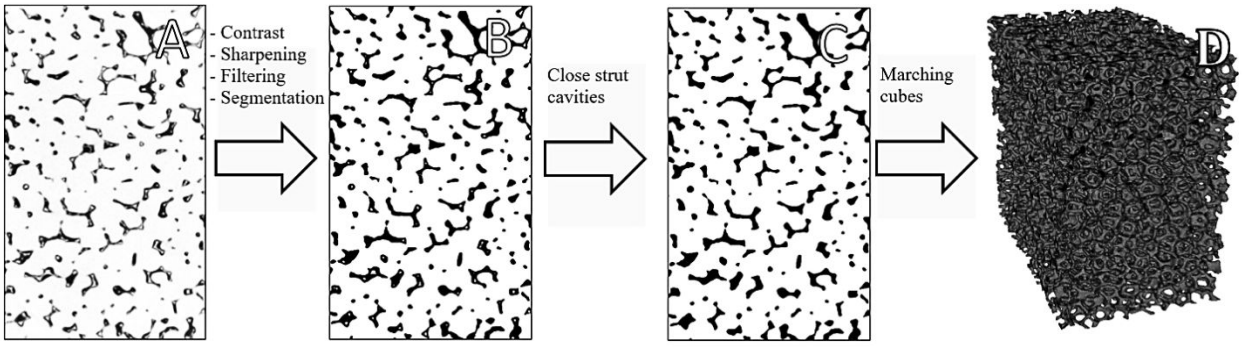

Figure 2. Image post-processing workflow: (A) 2D cross-sectional image from a 20 ppi SiSiC sample, (B) after image-enhancement and segmentation, (C) with closed strut cavities, and (D)

the final 3D model.

2.3 Determination of the representative elementary volume

The flow only needs to be simulated for a representative portion of the foam. This approach allows performing representative simulations at bearable computational costs. To this end, the Mean Representative Cubic Volume element (MRCV), which defines the smallest representative rectangular cuboid of the foam, is here determined. To evaluate the MRCV, the porosity (as an intrinsic property related to the geometrical structure) is computed over a range of increasing sub-volumes. This way, the local average quantities are statistically obtained.

To compute the porosity a voxel-based algorithm[16] was used. It divides the number of foreground (foam) voxels by the total number of voxels in the sub-volume. The porosities of the sub-volumes were evaluated in three different sections A, B and C as shown in Figure 3. This was done using the specific cubic-volume lengths (L_{MRCV}), defined as the length of one side of a cube) normalized with the sphere pore diameter (d_p)

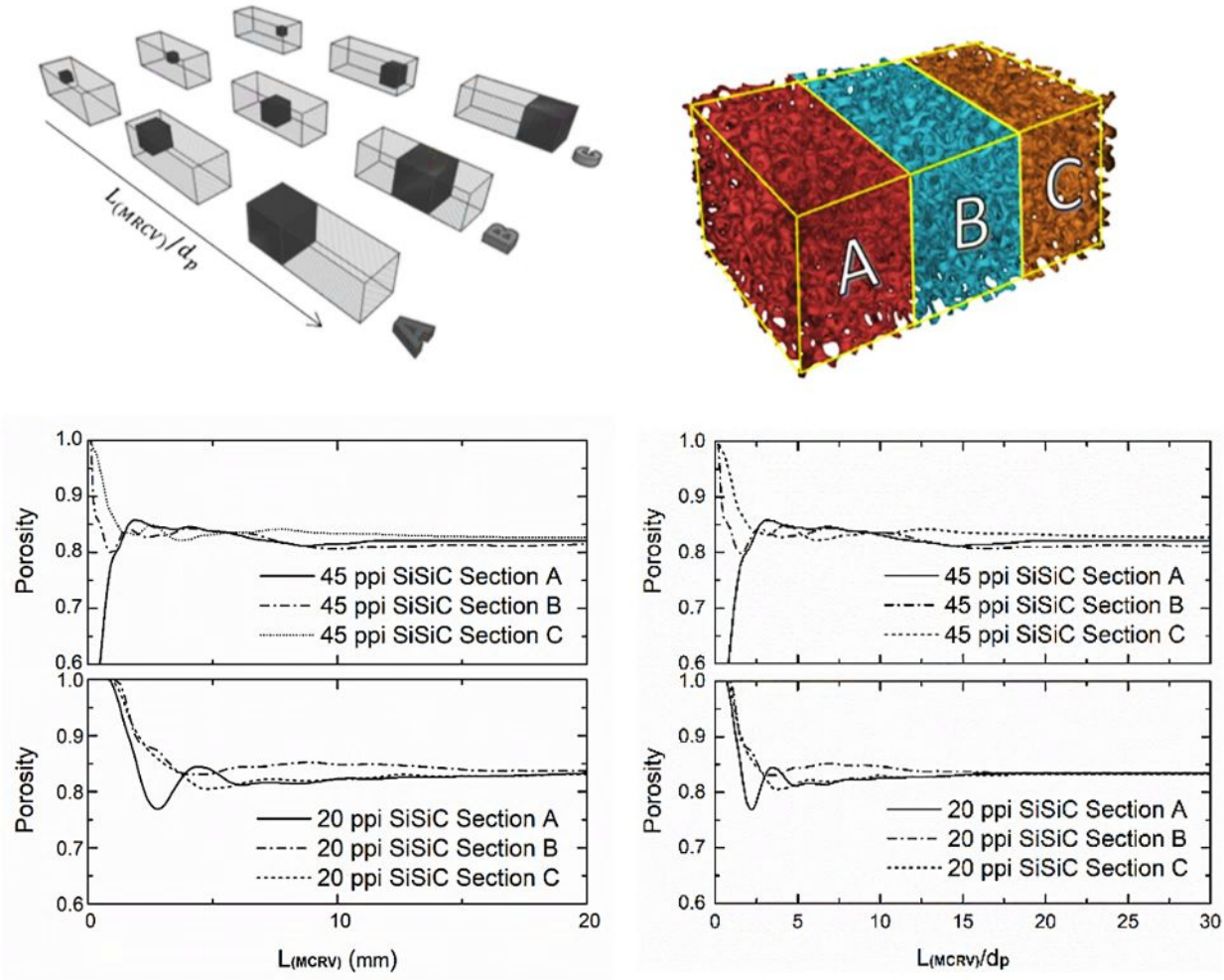

Figure 3. Determination of the representative cubic volume element of the foam.

The porosity value stabilizes with increasing L_{MRCV}. Hence, L_{MRCV} was set to 15 mm (20 ppi) and to 10 mm (45 ppi), respectively. This ensures that the porosity remained within ± 5% of the expected value.

3 Numerical modeling

3.1 Flow modeling

Single-phase flow for non-compressible gases is governed by the equations of continuity and conservation of inertial momentum given by

$$\nabla \cdot u = 0\,, \tag{8}$$

$$\frac{Du}{Dt} = -\frac{\nabla \mathrm{p}}{\rho} + \frac{1}{\rho}\nabla \cdot (\bar{\tau}) + g, \tag{9}$$

where ρ is the gas density, u the fluid velocity, $\bar{\tau}$ the summation of the viscous stress tensor and the turbulence stress tensor, and g the gravity acceleration. The CFD simulations were carried out using a Reynolds-averaged Navier-Stokes (RANS) turbulence model for a wide range of Reynolds numbers. The two equations associated with the RNG k-ϵ turbulence model are derived from the renormalization group theory as shown by Carvalho[17] according to

$$\frac{\partial}{\partial t}(k) + \frac{\partial}{\partial x_i}(ku_i) = \frac{1}{\rho}\left(\frac{\partial}{\partial x_i}\left(\alpha_k \mu_{eff}\frac{\partial k}{\partial x_j}\right) + G_k + G_b + \rho\varepsilon - Y_M + S_k\right), \tag{10}$$

$$\frac{\partial}{\partial t}(\epsilon) + \frac{\partial}{\partial x_i}(\epsilon u_i) = \frac{1}{\rho}\left(\frac{\partial}{\partial x_i}\left(\alpha_\epsilon \mu_{eff}\frac{\partial \epsilon}{\partial x_j}\right) + G_{1\epsilon}\frac{\epsilon}{k}(G_k + C_{3\epsilon}G_b) - G_{2\epsilon}\rho\frac{\epsilon^2}{k} - R_\epsilon + S_\epsilon\right), \tag{11}$$

where the inverse-turbulent Prandtl numbers (α_ϵ) and (α_k) are given by

$$\left|\frac{\alpha - 1.3929}{1 - 1.3929}\right|^{0.6321}\left|\frac{\alpha + 2.3929}{1 + 1.3929}\right|^{0.3679} = \frac{\mu_{mol}}{\mu_{eff}}, \quad (12)$$

where μ_{mol} is the molecular viscosity and μ_{eff} is the eddy viscosity. In the present work, temperature gradients and gravity are neglected ($G_b = 0$). The turbulent viscosity is given by

$$\frac{d\left(\frac{\rho^2 k}{\sqrt{\epsilon\mu}}\right)}{d(\hat{v})} = \frac{1.72\hat{v}}{\sqrt{(\hat{v})^3 - 1 + C_v}} \quad \text{with} \quad \hat{v} = \frac{\mu_{eff}}{\mu}. \quad (13)$$

At higher Reynolds numbers the production of turbulent kinetic energy (G_k) is given by

$$G_k = \mu_{eff} S^2, \quad (14)$$

while

$$G_k = \mu_t S^2, \quad (15)$$

$$\mu_t = \rho C_\mu \frac{k^2}{\epsilon} \quad (16)$$

at low-Reynolds numbers.

The Fluent commercial software package[18] includes a swirl modification function for the RNG model based on the modification of the turbulent viscosity

$$\mu_t = \mu_{t0} f\left(\alpha_s, \Omega, \frac{k}{\epsilon}\right), \tag{17}$$

where Ω is the swirl number, α_s is the swirl constant and $f(\alpha_s, \Omega, k/\varepsilon)$ is a function embedded the CFD program. In the RNG k-ϵ turbulence model, R_ϵ is defined as

$$R_\epsilon = \frac{C_\mu \eta^3 (1 - \eta/\eta_0)\epsilon^2}{(1 + \beta\eta^3)}, \tag{18}$$

$$\eta = S\frac{k}{\epsilon} = \frac{k}{\epsilon}\sqrt{2S_{ij}S_{ij}}, \tag{19}$$

where the applied closure coefficients are summarized in Table 1.

Coefficient	Value
a_s	0.07
C_μ	0.0845
C_v	100
G_b	0
$G_{1\epsilon}$	1.42
$G_{2\epsilon}$	1.68
η_0	4.38
β	0.012

Table 1. Splashing threshold criterions.

For a more apropriate simulation of the complex 3D flows, standard wall functions were also selected after comparing experimental and simulated pressure drop with

$$U^* = \frac{1}{\kappa} ln(y^*) + B \,, \tag{20}$$

where B = ln (9.793) and $U^* = u/u_\tau$ is normalized velocity in the near wall region divided by the shear wall velocity (u_τ), and $y^* = \rho u_\tau y/\mu$, in which y is the shortest distance to the wall and κ is the von Kármán constant.

3.2 Droplet modelling including motion, injection, evaporation by diffusion and wall interactions

The discrete phase model is a Lagrangian model valid for dilute flows with a particle volume fraction well below 10^{-5}.[18,19] In this model, the Eulerian gas phase is simulated as a continuum and the dispersed phase (single droplets) is solved by tracking a large number of droplets in a Lagrangian manner. The Euler-Lagrange approach is an appropriate numerical method widely used to simulate the transport of a dilute cloud of small liquid droplets. In this work, the droplet concentration is well below 10^{-5}, hence a one-way coupling assumption is sufficient[19]. A significant advantage of the Euler-Lagrange approach is the ease, with which the droplet impact/splash with the wall could be implemented. The implementation of the splashing using another multiphase flow method, such as the Euler-Euler[20], turned out to be much more difficult.

The droplets were here injected (dilute flow, volume concentration < 10^{-4}) and tracked after the flow simulation of the fluid phase had reached steady state. In this case droplets were treated as solid. The assumptions with respect to the droplet transport were as follows:

- droplets are spherical,

- molecular diffusion is neglected because the droplet diameter is here greater than 1 μm,

- droplets are surfactant-free,

- droplet-droplet interactions are neglected,

- droplet feedback on the gas phase is also neglected (one-way coupling),

- Because a one-way coupling is considered, no extra source term associated with the liquid-vapor surface tension needs to be included in the momentum equation. The liquid-vapor surface tension, however, is directly accounted for in the splashing criteria which is evaluated by the droplet impacting energy (Equation 36),

- gravity is neglected.

The Lagrangian equation of motions is given as

$$\frac{du_p}{dt} = F_D(u - u_p) + \frac{g_x(\rho_p - \rho)}{\rho_p}, \tag{21}$$

$$F_D = \frac{18\mu\, C_D Re_p}{\rho_p d_p^2 \;\; 24}, \tag{22}$$

$$Re_p = \frac{\rho d_p |u_p - u|}{\mu}, \tag{23}$$

$$C_D = a_1 + \frac{a_2}{Re_p} + \frac{a_3}{Re_p^2}, \tag{24}$$

where Re_p is the relative Reynolds number of a particle and C_D is an empirical drag coefficient used for calculating the drag force (F_D). For the computation of C_D, the coefficients a_1, a_2 and a_3 are empirical constants of smooth spherical particles given by Morsi.[21] For turbulent flow, the fluid velocity (u) is the summation of the mean fluid velocity ($\overline{u}$) and a fluctuation velocity (u'), calculated in accordance to a Discrete Random Walk Model[22] which relies on a Gaussian probability distribution of a random number (ζ) between 0 and 1, and a fluctuation component based on the turbulent kinetic energy defined as

$$u' = \zeta\sqrt{2k/3}, \tag{25}$$

which is known for each local point of the domain. Each particle position (x_p) is updated in time as

$$\frac{dx_p}{dt} = u_p. \tag{26}$$

The injection of droplets with a certain size distribution is performed using a Rosin-Rammler distribution function, where the mass fraction (Y) smaller than a given droplet diameter (d_d) is given by

$$1 - Y = exp\left[-\left(\frac{d_d}{d_n}\right)^{n_d} \right], \quad (27)$$

where d_n is the diameter size constant and n_d the size distribution parameter. In a first numerical test, uniform droplets with dimeters of 10 µm, 50 µm or 100 µm were considered. In a second test, the droplet size was specified as multiple-size droplet injection according to a Rosin-Rammler droplet size distribution $Y_d = \exp\ -\left(\frac{d_d}{61.269}\right)^{4.017}$, which was selected to be close to a Gaussian distribution ($R^2 = 0.9983$). Table 2 summarizes the mass fractions of respective droplet sizes.

Diameter range (µm)	Mass fraction (%)
10-15	0.35
15-25	2.34
25-40	13.80
40-55	28.73
55-70	36.64
70-85	15.71
85-95	2.11
95-100	0.29
Total	100

Table 2. Mass fractions for the multi-size droplet injection.

Droplets at ambient temperature and pressure vaporize by diffusion. The molar vapor flux (N_i) that a droplet loses by diffusion is calculated as

$$N_i = k_c \Delta C \,, \tag{28}$$

$$k_c = \frac{\left(2 + 0.6 Re_d^{0.5} Sc^{\frac{1}{3}}\right) D_{vap}}{d_d}, \tag{29}$$

where ΔC is the vapor concentration difference between the bulk gas and the droplet surface, k_c is the mass transfer coefficient, and D_{vap} is the diffusion coefficient of vapor.

Droplet-wall interactions are known to depend on the impaction regime, which is represented by the Weber number (ratio of inertial forces to surface tension forces) and the Ohnesorge number (ratio of viscous forces to surface tension forces), respectively defined as

$$We = \frac{\rho_L v^2 d_d}{\sigma_{lv}}, \tag{30}$$

$$Oh = \frac{We^{1/2}}{Re} = \frac{\mu}{(\rho_L \sigma_{lv} d_d)^{1/2}}. \tag{31}$$

After the impact of a droplet with a non-heated dry rigid surface has occurred, the droplet can either deposit (i.e. the total mass of the droplet remains attached to the surface) or splash (i.e. the droplet breaks up and produces a rim of fluid ejecting smaller droplets). A widely used threshold criterion (K_s) to distinguish between deposition and splashing was proposed by Stow[23] and confirmed experimentally by Mundo et al.[24] as

$$K_s = Oh^{\alpha} Re^{\beta} . \quad (32)$$

For rough surfaces Mundo et al.[24] suggested α = 1, β = 5/4 and K_s=57.7, while Rosa et al.[25] suggested α = 8/5, β = 2 and K_s=3.5. Later Roisman[26] analyzed empirical data from previous investigations and proposed two boundary conditions for the droplet impact leading to a secondary droplet formation with the capillary number (Ca) and Ohnsorg number defined as

$$Ca = 0.067 + 0.6\, Oh^{0.35} , \quad (33)$$

$$Oh = 0.0044 , \quad (34)$$

respectively. Roisman[26] studied the droplet splashing on rough and porous ceramic substrates manufactured via sintering process. He found that the splashing on such substrates are material independent. Irrespective of the contact angle[26,27] (for non-super-hydrophobic or super-hydrophilic)[28], the splashing was found to only depend on the characteristic slope morphology (R_{pk}/RS_m) and the initial inertial forces in terms of the Weber number for the splashing thresholds (We_S) as

$$We_S = 10.5(R_{pk}/RS_m)^{-0.7} = 41.885(R_z * RP_c)^{-0.7603} . \quad (35)$$

For non-super hydrophobic and hydrophilic materials (the droplet splashes when $We > We_S$). In Eq. 35, R_{pk} is the average height of the protruding peaks above the roughness core profile, RS_m is the mean width of a profile element, R_z is the maximum height profile and RP_c is the standardized number of peaks.

According to Gipperich,[29] porous ceramics have surface roughness parameters ranging from $R_{z,min} = 0.0003\ cm$ $(RP_{c,min} = 32\ peaks/cm)$ to $R_{z,min} = 0.0113\ cm$ $(RP_{c,min} = 152\ peaks/cm)$, which results in We_S of 1431.64 to 27.76. Using the thresholds proposed by Gipperich,[29] Mundo[24] and Roisman,[26] a splashing/deposition figure was produced (see Figure 4) to distinguish between splashing and deposition.

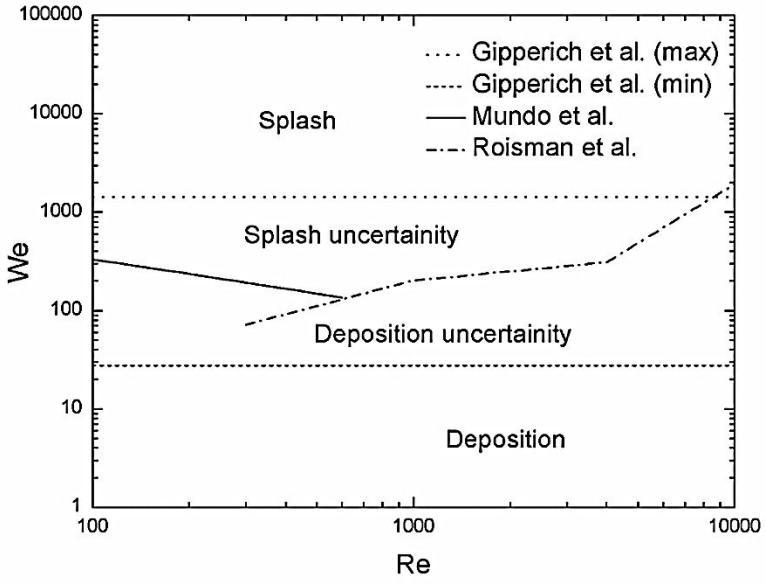

Figure 4. Splashing and deposition thresholds for porous ceramics.

In accordance with Figure 4 from We = 28 to We = 1433 the splashing or deposition is uncertain for the SiSiC material. In this work those uncertainties were treated as certain splashing or deposition, respectively using the thresholds defined by Mundo[24] and Roisman.[26] Re-entrainment of deposited droplets was not considered in this study.

In cases, which coincide with the deposition region, a trap boundary condition for the discrete phase was used. Else, the splash of small droplets was implemented. The implemented user-

defined functions (UDF) are described below. To distinguish between deposition and splashing, the impact energy (E) is calculated as

$$E^2 = \frac{We}{\left(min\left(\frac{h_0}{d_p},1\right) + \frac{1}{\sqrt{Re}}\right)}, \quad (36)$$

where h_0 is the film height (for dry surfaces $h_0 = 0$), d_p is the droplet diameter, We is the Weber number and Re is the Reynolds number. Using Mundo[24] and Roisman.[26] thresholds (see Figure 4) the corresponding quadratic minimum splashing energy (E_s^2) were calculated as

$$\begin{array}{ll} E_s^2 \geq 3329 & \text{for } Re \leq 600 \\ E_s^2 \geq 0.18Re^{1.5} + 22.6Re^{0.5} & \text{for } 600 < Re \leq 1000 \\ E_s^2 \geq 4.62Re^{1.5} - 624.36Re^{0.5} & \text{for } 1000 < Re \leq 4000 \\ E_s^2 \geq 2x10^{-5}Re^{2.5} - 3x10^{-15}Re^{1.5} + 9x10^{-12}Re^{0.5} & \text{for } Re > 4000 \end{array}. \quad (37)$$

a) Deposition:

Trapped boundary condition (i.e. $v_{2,n}$=0) is achieved when the energy upon collision with a wall is lower than the minimum splashing energy ($E^2 \leq E_s^2$) given by (Eq. 37).

b) Splashing:

Upon splashing ($E^2 \geq E_s^2$), a portion of the droplet remains on the wall, and subsequently, smaller droplets re-enter the gas flow. To determine the mass fraction (M/M_0, where M is the droplet mass re-entering the gas flow and M_0 is the initial mass of the droplet impacting with the

surface) of a spray of smaller droplets (also termed splashed droplets), the correlation of O´Rourke[30] was used as

$$\frac{M}{M_0} = \begin{cases} 1.8x10^{-4}\left(E^2 - E_{crit}^2\right) & \text{for } E_{crit}^2 = 57.7^2 < E^2 < 7500 \\ 0.75 & \text{for } 7500 < E^2 \end{cases} . \quad (38)$$

To determine the diameter distribution of the splashed droplets, a Weibull probability density function $f(d_d;D,2))$ is used as

$$f(d;D,2) = 2\frac{d}{D^2}e^{-(d/D)^2}, \quad (39)$$

where d_d is the random variable (in this case, the droplet diameter), D is known as the distribution shape parameter and 2 is the scale parameter (fitted to data from Mundo et al.[31]). The corresponding cumulative probability function and the maximum diameter of the splashed droplet (in accordance with O'Rourke[30]) are then given by

$$F(d_d;D,2) = 1 - e^{-\left(\frac{d_d}{D}\right)^2}, \quad (40)$$

$$\frac{d_{d,max}}{d_{d,incident}} = \left(\frac{57.7^2}{E^2}, \frac{6.4}{We}, 0.06\right). \quad (41)$$

The total number of ejected droplets that re-enter the gas flow can be calculated with the splashed mass fraction from Eq. 38 as

$$\frac{\rho\pi}{6} N_{tot} \sum_{n=1}^{N_{parcels}} \left(f_n d_n^3\right) = M \,, \tag{42}$$

where N_{tot} is the total number of splashed drops and $N_{parcels}$ is the number of splashed drops per parcel, where parcels are statistical representations of a number of individual droplets.

Finally, to calculate the velocity, at which the smaller droplets are splashed off from a wall surface, a second Weibull function fitted to data of Mundo[24] was used according to

$$f\left(\frac{V_{normal,splashed}}{V_{normal,incident}}; \emptyset_v, b_v\right) = \frac{b_v}{\emptyset_v}\left(\frac{V_{normal,splashed}}{V_{normal,incident} \cdot \emptyset_v}\right)^{b_v - 1} e^{-\left(\frac{V_{normal,splashed}}{V_{normal,incident} \cdot \emptyset_v}\right)^{b_v}} \,, \tag{43}$$

$$\frac{V_{normal,splashed}}{V_{tangential,splashed}} = tan(65.4 + 0.226\emptyset_l) \,, \tag{44}$$

where b_v and $\emptyset_v$ are given as

$$b_v = \begin{cases} 2.1 & if\ \emptyset_l \leq 50° \\ 1.10 + 0.02\emptyset_l & elsewhere \end{cases} \,, \tag{45}$$

$$\emptyset_v = 0.158 e^{0.017\emptyset_l} \,. \tag{46}$$

3.3 Residence time distributions model

The residence time distribution function ($E(t)$) describes the distribution of droplet that has spent a given time in a section of the foam volume. It is here obtained using CFD to track the droplets at the exit of the foam.[32] In this case, $E(t)\delta t$ is the fraction of droplets exiting the foam, which spent time between t and $t + \delta t$ inside the foam. The histogram of time at the outlet is the $E(t)$ defined as

$$E(t) = \frac{C(t)}{\int_{t=0}^{\infty} C(t)dt}. \tag{47}$$

The average residence time (τ_i) of the ith droplet is calculated as

$$\tau_i = \frac{\int_0^{\infty} tC(t)dt}{\int_0^{\infty} C(t)dt}. \tag{48}$$

The mean residence time (τ) is computed by averaging the residence time of each particle as

$$\tau = \frac{\sum_{i=1}^{N} \tau_i}{N}. \tag{49}$$

The global residence time distribution ($f_n(t)$) for multiple integers of individual sections is computed using the convolution of each RTD functions ($E_n(t)$) according to

$$f_n(t) = E_1(t) \otimes E_2(t) \otimes \ldots \otimes E_n(t)\,. \tag{50}$$

The function $f_2(t)$ reads for example as

$$f_2(t) = E_1(t) \otimes E_2(t) = \int_{-\infty}^{\infty} E_1(\theta) E_2(t-\theta) d\theta. \tag{51}$$

A convolution is the response of a system to any pulse. The response to a pulse acting at time (θ) is the shifted impulse response ($E(t-\theta)$) multiplied by the area of the pulse.

3.4 Resolved CFD mesh of the foam

3D surface meshes (of both the 20 ppi and the 45 ppi SiSiC foam portions) were first generated using the marching cubes algorithm[33] for the extraction of iso-surfaces from the scanned foam volume (in the present case, the 3D foam volume was discretized into a set of voxels). In a second stage, the meshes were simplified using an edge-collapse decimation algorithm[34] thereby preserving boundaries, topologies, and also the normal directions of the mesh surfaces. The obtained meshes were then smoothed using a Laplacian operator,[35] holes were flat-filled, small non-connected structures were eliminated, sharp spikes were flattened, and the fluid domain was generated. Finally, the CFD meshes were generated using an unstructured grid algorithm with curvature-based grid-refinement. The produced tetrahedral meshes were suitable for the CFD simulations. The skewness ratios (min/max) were 0.014 and 0.021 for 20 ppi foam and 45 ppi, respectively.

The boundary conditions needed for the CFD simulation are summarized in Table 3 and illustrated in Figure 5.

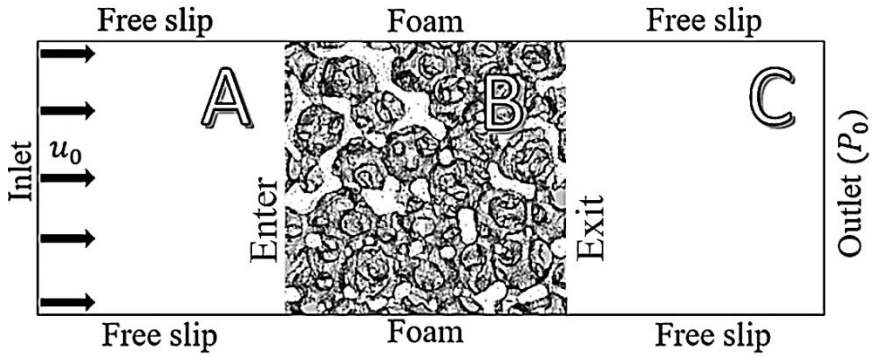

Figure 5. 2D schematic of the CFD domain: A - inlet fluid surface B - foam domain, C - outlet fluid surface.

Interface	Velocity	Pressure	Zone
Inlet	$\frac{\partial u}{\partial x} = \frac{\partial u}{\partial y} = \frac{\partial u}{\partial z} = 0$	Calculated	A
Outlet	$\frac{\partial u}{\partial x} = \frac{\partial u}{\partial y} = \frac{\partial u}{\partial z} = 0$	P = 0	C
Walls (free slip)	$\frac{\partial x}{\partial z} = \frac{\partial y}{\partial z} = u = 0$	$\frac{\partial P}{\partial x} = \frac{\partial P}{\partial y} = 0$	A, B and C
Foam (no slip)	$u\|_{(y^+ = 0)} = 0$	Calculated	B

Table 3. Boundary conditions used for the CFD simulations.

To avoid influence of flow entrance and exit effects in the CFD simulations, the inlet and outlet mesh surfaces were positioned further upstream and downstream with a distance equalled to 70% of the foam streamwise length.

3.5 Mesh size and turbulence model

For the CFD flow simulations, the governing Equations (Eq. 8 to 20) were solved with a finite volume method (FVM). The CFD convergence criterion was set to 10^{-4} for the scaled residuals. To ensure good accuracy of the numerical results, a grid dependence study was conducted with the 45 ppi foam mesh by varying the maximum cell length segment from 0.1 mm to 0.065 mm with a constant minimum cell length segment of 10^{-3} mm. The convergence study was also performed for superficial gas velocities (U_{GS}, the velocity of the flow in a given cross sectional area) ranging from 0.1 to 1.0 m/s which corresponds to Kozeny-Carman Reynolds numbers (Re_1) ranging from 6.6 to 66.2, respectively. The pressure drop was also used as an evaluation criterion (see Table 4). With a maximum cell length segment of 0.08 mm, the highest percentage error was below 8% from the experimental value. The variation from 0.08 mm to 0.065 mm results in less than 3% of the pressure drop change. In all subsequent simulations, grids with a cell length segment of 0.08 mm were used.

Max. cell length segment (mm)	Nodes (/10^6)	Pressure drop (Pa/m)		
		U_{GS} = 0.1 (m/s)	U_{GS} = 0.5 (m/s)	U_{GS} = 1.0 (m/s)
0.1	1.15	146.8	1061	3000
0.09	1.44	141.8	1067	3036
0.08	1.92	142.5	1082	3087
0.07	2.39	143.5	1108	3187
0.065	2.86	143.7	1107	3164
Experimental value		142.7	1136.4	3339.4

Table 4. Grid dependence study.

The effect of the turbulence model was also tested for the 45 ppi foam. The simulated pressure drops were compared with their experimental counterparts in Table 5. The experimental study was accomplished with SiSiC open-cell foams of 20 ppi and 45 ppi having sample lengths of 100 mm. All experimental measurements of the pressure drop were carried out at atmospheric pressure and at ambient temperature. The inlet superficial gas velocity was varied between 0.1 and 1.7 m/s. The two turbulence models (the RNG k-ϵ model with standard wall functions and that with the swirl modification) provided the best agreements with the experimental data. A graphical visualization of the flow is shown in Figure 6.

Turbulence Model	Pressure drop (Pa/m) at U_{GS} = 1.7 (m/s)
k- ε	7977
RNG k-ε, standard wall functions	7900
k-Ω	7635
RNG k-ε, enhanced wall functions	7431
Experimental	7800

Table 5: Pressure drop for 45 ppi foam depending on the selected turbulence model. The RNG k-ε with standard wall functions performs best.

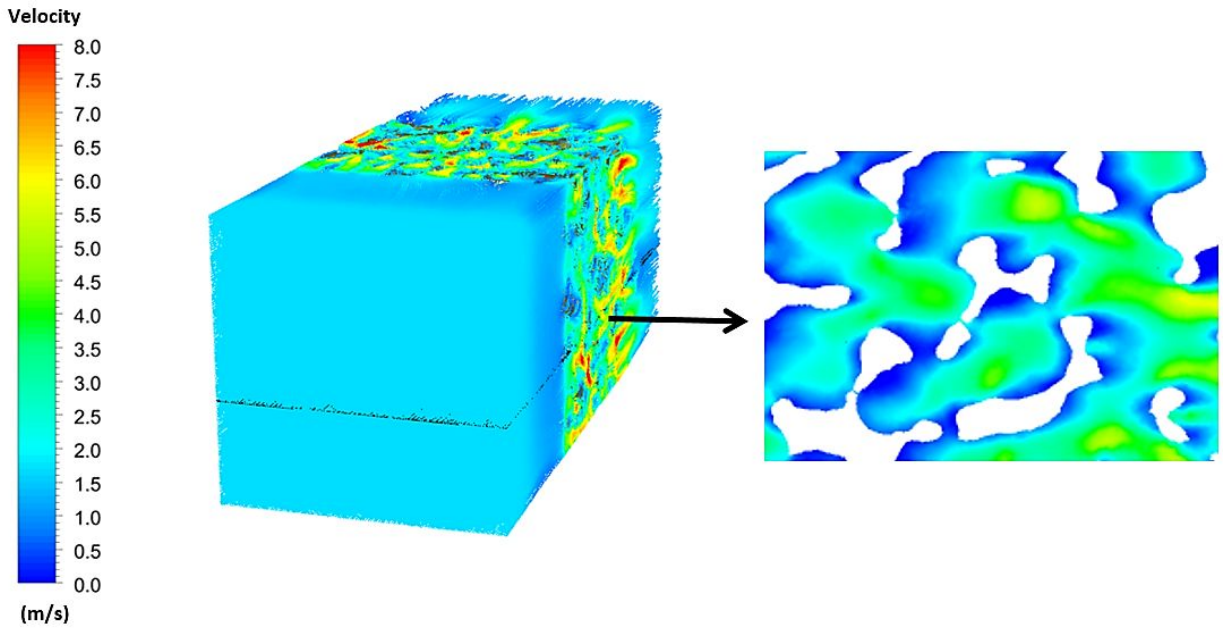

Figure 6: 3D (left) and 2D (right) visualizations of the simulated velocity for single phase flow (45 ppi foam, U_{GS} = 1.7 m/s). The 2D horizontal cross-sectional plane a mid-section of the 3D flow volume.

4 Results and discussion

4.1 Foam structure

The foam porosities (ε) reported from the manufacturer (ε_{manuf}), and those calculated from the pre-processed data (ε_{pre}), from the post-processed CFD mesh (ε_{post}), as well as the pore equivalent diameter (d_p) and strut diameter (d_s) were determined from the post-processed tomographic data (See in Table 6).

ppi	S_v (m^2/m^3)	ε_{manuf}	ε_{pre}	ε_{post}	d_p mean (µm)	d_p max. (µm)	d_s (µm)

20	2000	0.87	0.871	0.836	2399.94 ± 380.15	3743.75	390.86 ± 153.56
45	1004	0.85	0.861	0.821	1036.13 ± 125.56	1437.64	248.80 ± 94.77

Table 6. Morphological foam properties (pre-processed d_p and d_s are not shown, since cavities in the interior of struts interfere with the measurements providing incorrect results).

The porosities computed from the pre-processed tomographic datasets are in excellent agreement with the values reported by the manufacturer. The slight differences are likely attributed to losses in the topological morphology from X-ray scanning and 3D reconstructions. As expected, the porosity of the post-processed tomographic data is slightly smaller due to filled cavities, decimation and Laplacian smoothing.

Both, pore and strut diameter distributions of the post-processed data were calculated using the diameter of the largest spheres that fits inside them as described by Hilderbrand,[36] using the Dougherty's algorithm.[37] The mean pore diameter varied between 1.0 and 2.4 mm across all the investigated foams. The equivalent strut diameter was on average more than five times smaller than the mean pore size.

4.2 Comparison of the pressure drop

For comparison purposes, the pressure drop was modeled using a modification of the Ergun equation (Eq. 4), which was extended to open-cell foams.[38] In this model, the sphere particle diameter used in the original Ergun equation is replaced with the inverse specific surface area ($1/S_v$) of the foam. As a result, the modified Ergun equation for SiSiC foams (R^2=0.9957 and Rmsd=17.12) is

$$\Delta p = 559.6\frac{(1-\varepsilon)^2 S_v^2 \mu_L}{\varepsilon^3} v_f + 2.5\frac{(1-\varepsilon) S_v \rho_L}{\varepsilon^3} |v_f| v_f \,. \quad (52)$$

The pressure drop calculated using the modified Ergun model in Eq. 52 is compared with the experimental data (including experimental data of a 30 ppi SiSiC foam) in Figure 7. The pressure drop is shown as a function of the modified Kozeny-Carman Reynolds number (Re_1) defined as

$$Re_1 = \frac{\rho U_0}{(1-\varepsilon) S_v \mu} \,. \quad (53)$$

The macroscopic flow regimes "viscous and inertia regime" were considered to describe both the turbulent (Re_1>100)[39] and the laminar (Re_1<100) flow in the porous. The model fit is generally excellent. It only tends to overestimate the predicted pressure drop at bigger pore sizes or as turbulence increases, which is related with the determined dimensionless parameters α and β, which should not have a constant value, instead these parameters should be functions of the foam geometry that is different for every pore density.

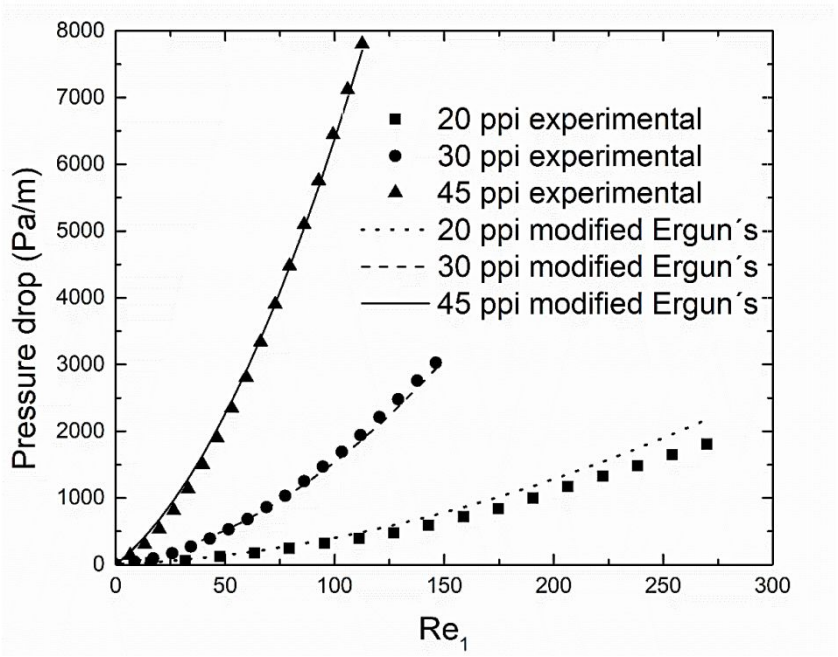

Figure 7. Comparison between predicted pressure drop (Eq. 52) and experimental values.

The CFD calculations were also compared against the data obtained from the Lacroix model (Eq. 5), from the Du Plessis model (Eq. 6), from the modified Ergun's model (Eq. 52), and from experimental pressure drop data (see Figure 8). The calculated CFD pressure drop is most accurate compared with the experiments since the real foam structure is resolved.

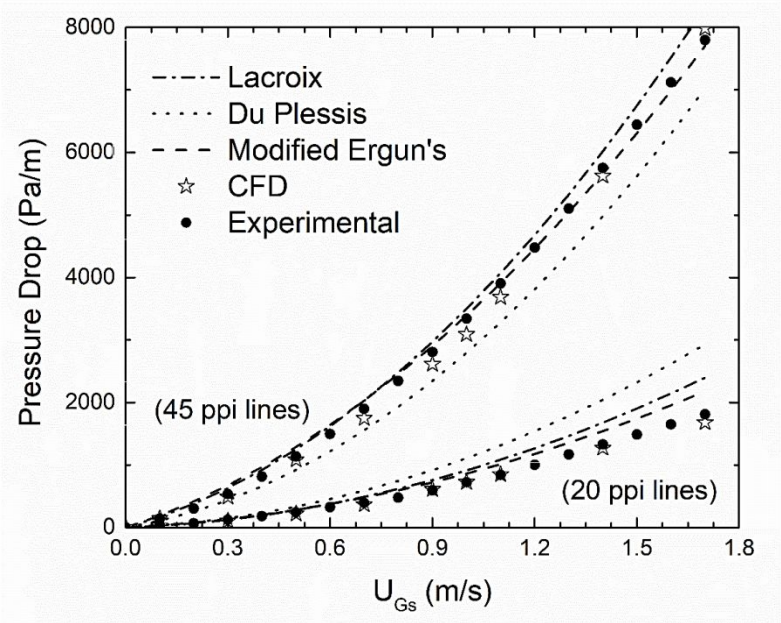

Figure 8: Comparison between correlated, experimental and simulated (CFD) pressure drop values for 20 ppi and 45 ppi foams.

4.3 Effect of pore density and superficial gas velocity on droplet residence time

The droplet RTD curves were obtained from the injected droplets and those exiting the foam. The RTDs were smoothed using weighted adjacent-averaging and then fitted with a modified Dagum distribution with the five fitting parameters (k,α,β,γ and ζ) according to

$$E(t)(t;k,\alpha,\beta,\gamma,\zeta) = \frac{\alpha k\left(\frac{t-\gamma}{\beta}\right)^{\alpha\zeta-1}}{\beta\left(1+\left(\frac{(t-\gamma)}{\beta}\right)^{\alpha}\right)^{k+1}}. \quad (54)$$

The droplet RTDs are shown in Figures 9 to 11. The parameters associated with the fitted Dagum RTD are summarized in the Supporting Information (see Table S1).

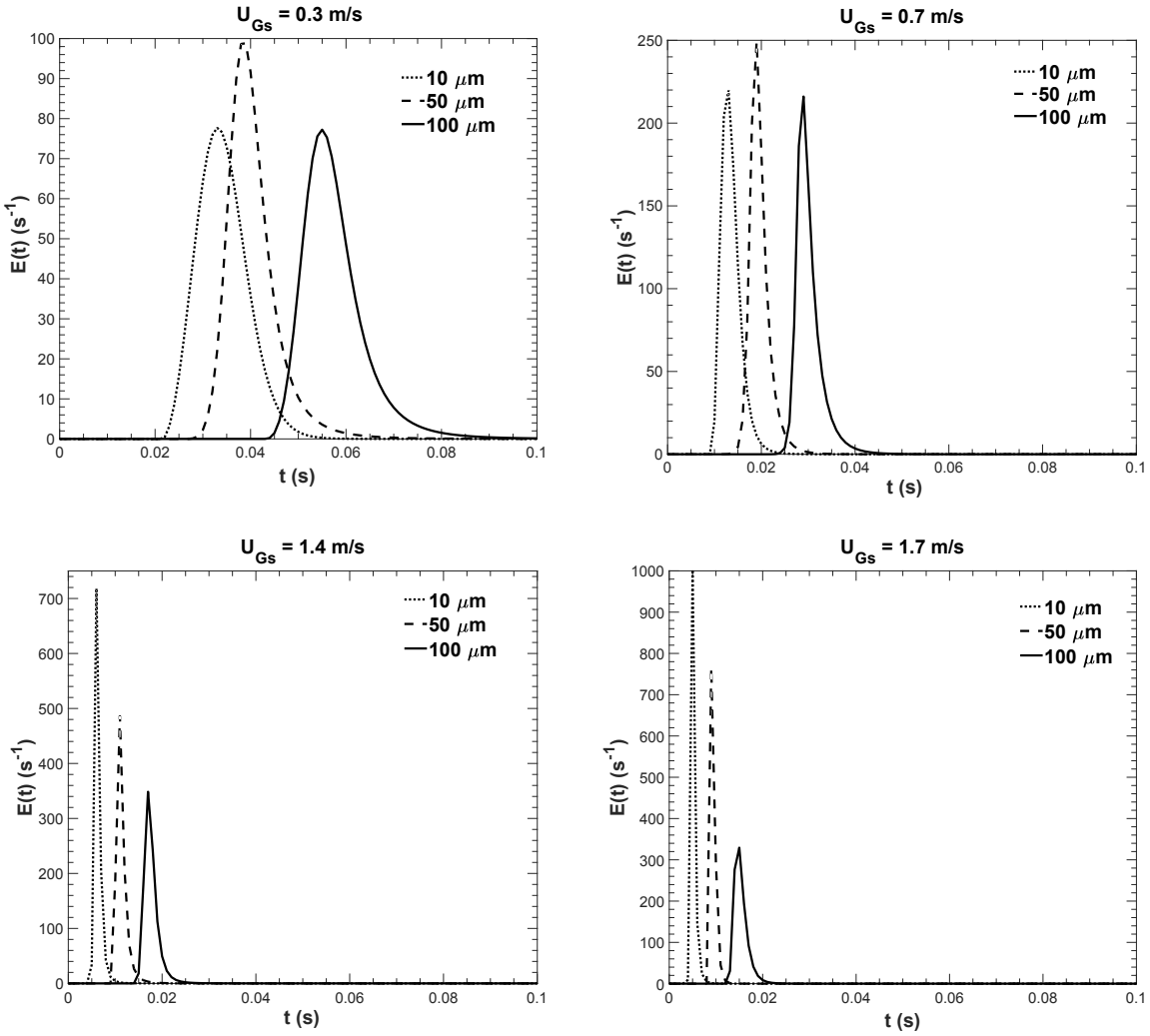

Figure 9. Droplet RTD curves $E(t)$ computed from the CFD simulations at different frontal superficial gas velocities (U_{GS}) and droplets sizes for the foam with a pore density of 20 ppi. The foam length is 15 mm.

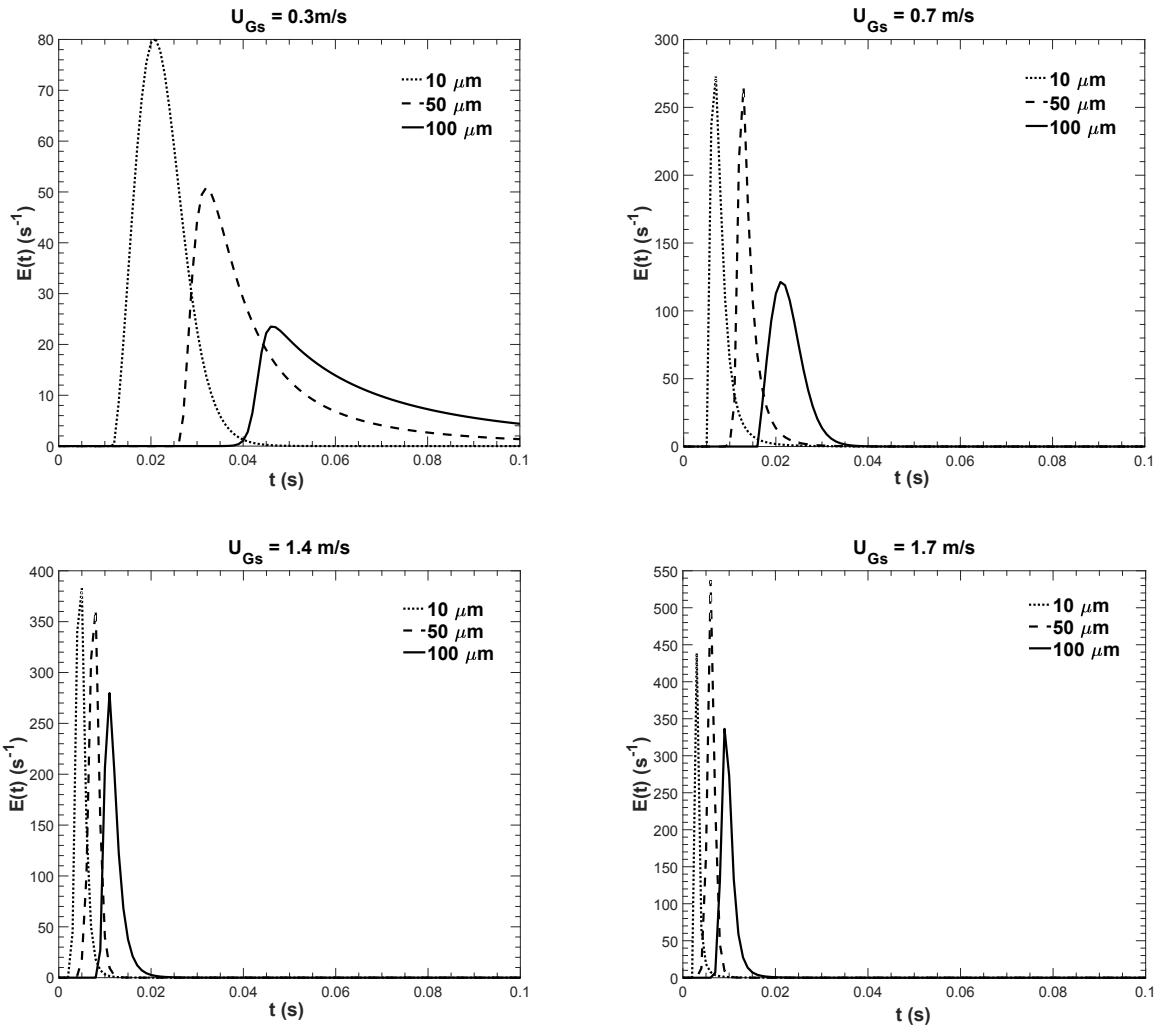

Figure 10: Droplet RTD curves $E(t)$ computed from the CFD simulations at different frontal superficial gas velocities (U_{GS}) and droplets sizes for the foam with a pore density of 45 ppi. The foam length is 10 mm.

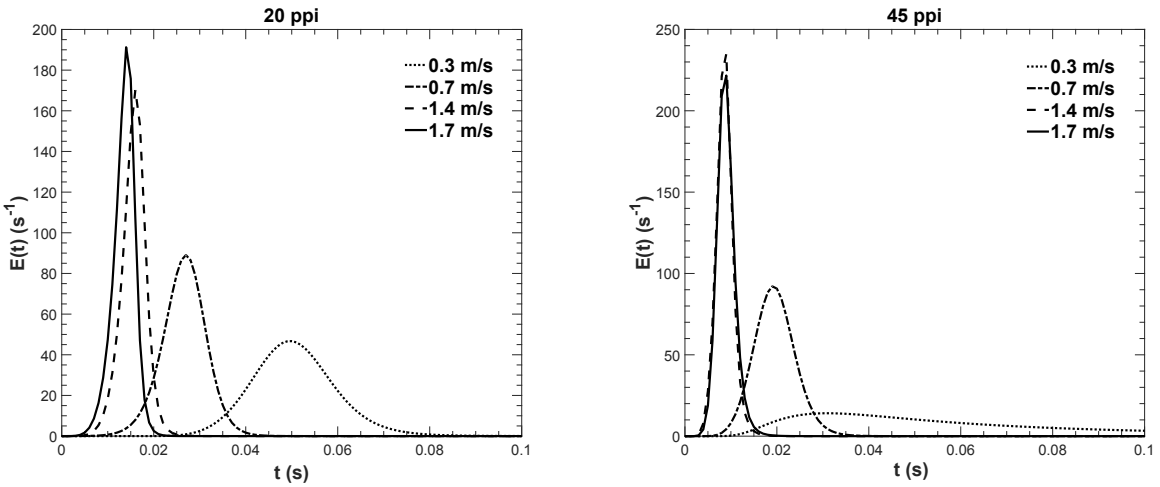

Figure 11: Droplet RTD curves $E(t)$ computed from the CFD simulations at different frontal superficial gas velocities (U_{GS}) for Rosin-Rammler droplets; the foam lengths are 15 mm (right) and 10 mm (left).

As seen in Figures 9 to 10, the larger the droplets are, the longer they remains within the foam. Droplets with smaller inertia are easily carried with the fluid and have less interactions with the foam skeleton compared with bigger droplets, in particular at low superficial gas velocity (see Figure 11). It should be noticed that the droplet size is continuously reduced by diffusion, which allows a faster passage of the foam.

To compare the residence time of 20 ppi and 45 ppi foams (see Figure 12), both Dagum RTDs were scaled to a foam length of 30 mm using the convolution of distributions (Eq. 50). The droplet inertias ($S \cdot d_d^2 \rho_d / 18\mu_L$), where the density ratio $= \rho_p/\rho_g = 829$, are 0.45 s, 0.115 s and 0.0046 s for droplet diameters of 100 µm, 50 µm and 10 µm, respectively. The RTDs in Figure 12 are shown in terms of so-called box-plots, which graphically show the droplet spectra through their statistics quartiles. No significant difference in the residence time is observed for the

smallest droplet inertia (0.0046 s) in foams with pore densities of 20 ppi (d_p = 2.4 mm) and 45 ppi (d_p = 1.0 mm). Droplets with diameters below 10 μm are unaffected by the foams since the droplet size is significantly smaller than the mean foam pore size (d_p/d_d = 240). For droplets with diameters beyond 50 μm, there is a significant difference between the times droplets are retained within the foam, which increases with decreasing mean pore size ($d_p/d_d \leq 48$).

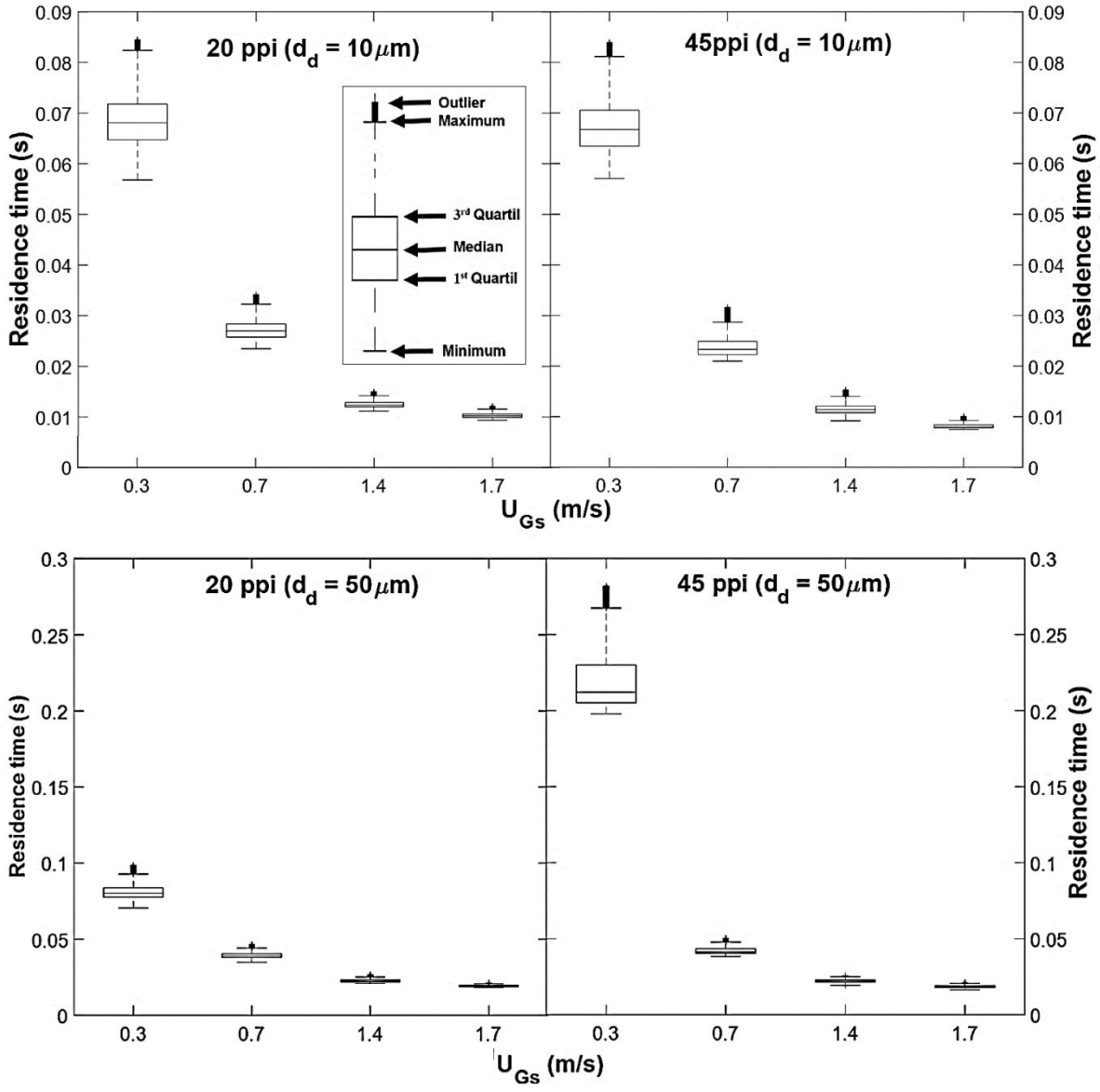

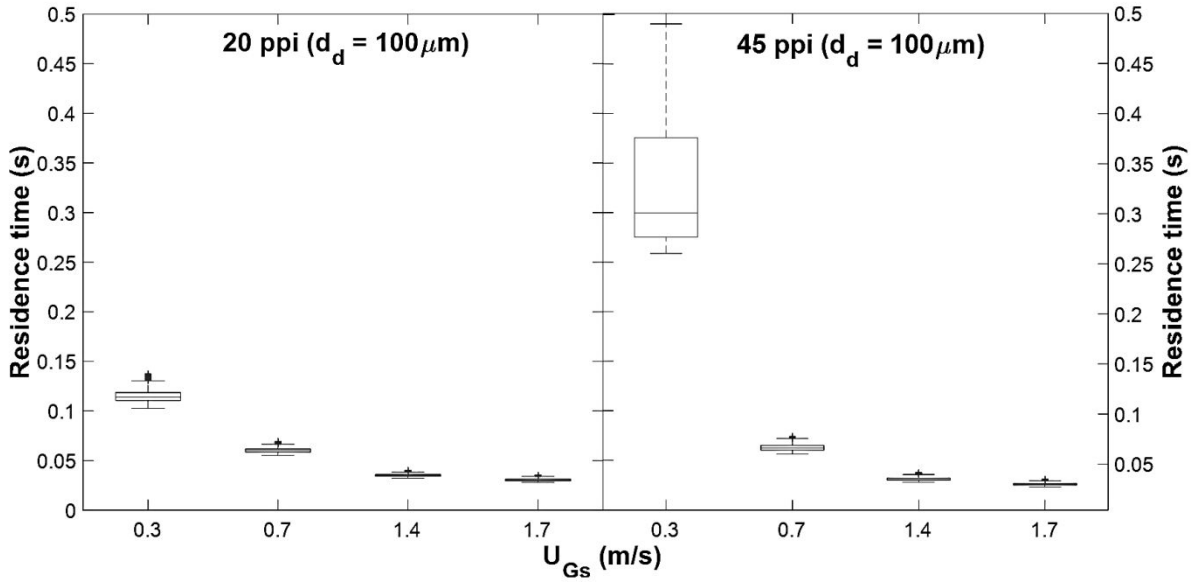

Figure 12. Box-plots of the droplet RTDs at different frontal superficial gas velocities (U_{GS}) and droplets sizes for foams of 30 mm length with pore densities of 20 ppi (right) and 40 ppi (left).

4.4 Effect of pore density and superficial gas velocity on droplet separation.

The percentage of droplets escaping and of those trapped (trapped droplets are those who crashed against a surface of the foam) are shown in Figure 13 (evaporated droplets are intentionally not included). Splash-generated droplets are considered as well in the trapped and escaped categories. The pore density of the 20 ppi foam allows for more droplets to escape than the 45 ppi foam. The 20 ppi foam has less specific surface, it hence implies a lower probability of droplet impact with the foam skeleton. It is also shown that an increase in the superficial gas velocity results in a decrease of the percentage of droplets escaping the foam, accordingly. This can be explained by the fact that, as the droplet inertia increases, the motion of droplets resist longer to the entrainment effect of the long-lived flow patterns within the foam structure. As

droplets are dominated by their inertia the trajectories they follow decrease avoiding impacts with the foam skeleton.

For both pore densities, there is not significant difference in the number of droplets escaping the foams for injected droplets with diameters greater than d_d > 50 μm in both laminar and turbulent flows (maximum U_{GS} = 17 m/s). When the droplets with 10 μm - diameter were injected, the percentage of droplets escaping the foam is considerably larger compared with the larger droplets. Such that the foam with a pore density of 20 ppi allows, 84.5 % of droplets to pass through its structure without crashing with the foam.

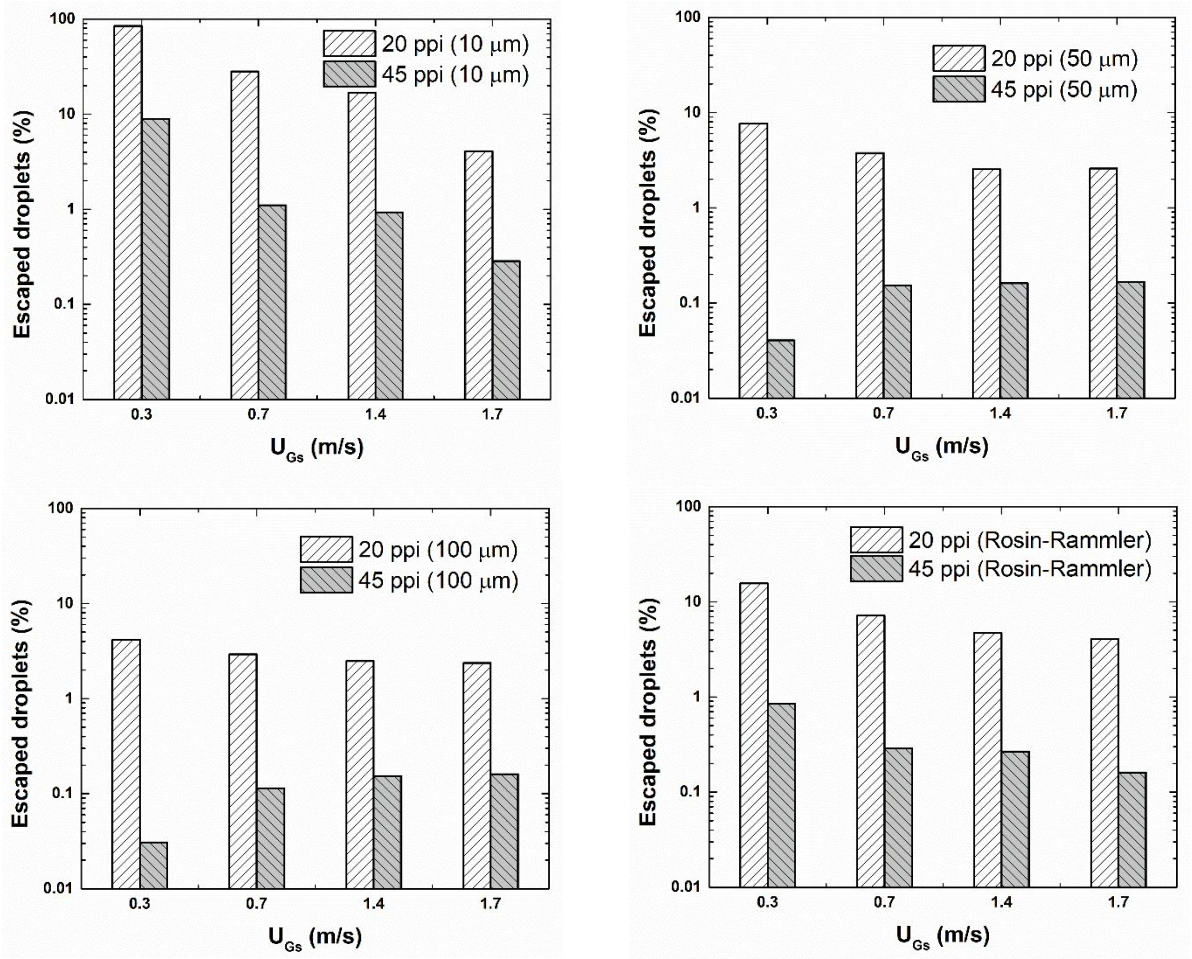

Figure 13. Percentage of droplets escaping the foams for injected droplet size of (left-top) 10 μm, (right-top) 50 μm, (left-bottom) 100 μm and (right-bottom) the Rosin-Rammler distribution.

5 Conclusions and outlook

Inline droplet separation devices composed of open-cell ceramic foams are promising. In the present work, the residence time distribution of droplets and the separation efficiency of open-cell foams was studied using a numerical approach. Numerical findings were reported considering the pressure drop and the residence time distribution of droplets within foams under different superficial flow velocities, foam densities of 20 and 45 ppi, and different droplet inertia by injections of droplets with diameters of 10 μm, 50 μm and 100 μm. The main results from this work are:

- For the pore-to-droplet diameter ratio $d_p/d_d \leq 50$, the droplet residence time increases with the pore density. For practical applications, we recommend foams with high pore density, as they exhibit a better separation performance.

- For $d_p/d_d \geq 240$ and with a superficial gas velocity lower than 1.7 m/s, no significant difference in the droplet residence time exists between open-cell foams with pore density between 30 and 45 ppi. Under these conditions, there is no observable enhancement in droplet separation between different foams pore densities.

- The probability of droplet impact with the foam skeleton increases with increasing superficial gas velocity.

- The porosity of SiSiC foams becomes constant for non-dimensional lengths $L_{MRCV}/d_p > 15$ (L_{MRCV}/d_p, where $MRCV$ is the Representative Cubic Volume element). This allows highly accurate pressure drop predictions using CFD simulations.

Other porous SiC foams (i.e. foam used by Lacroix[8]) and SiSiC exhibit both a similar skeletal network and a similar triangular strut shape[7], if they are sintered using the same fabrication technique. The presented conclusions on droplet retention time will therefore also apply to similar SiC foams that have a similar pore size and pore porosity.

Future work will deal with the overall comparison of residence times and droplet separation efficiency with experimental data and investigations at higher Kozeny-Carman Reynolds number $Re_1 > 300$ (See Eq. 53). Further correlations of the relevant quantities, such as RTD and droplet separation efficiency will be derived by performing additional simulations over a wider range of pore densities and superficial gas velocities. Finally, comparisons with experimental data on the diameter of the droplet escaping the foam will be performed. Droplet splashing at high Reynolds number plays a major role in the separation and will be further analyzed in the future.

Acknowledgment

The financial support from Consejo Nacional de Ciencia y Tecnología - CONACYT (scholarship number: 91681100) and from German Academic Exchange Service - DAAD (scholarship number: 470810) are gratefully acknowledged.

Nomenclature

A	Pore diameter, m
C	Forchheimer coefficient, m^{-1}
Ca	Capillary number
d_p	Sphere pore diameter or equivalent pore diameter, m
d_d	Sphere droplet diameter or equivalent particle diameter, m
d_s	Strut diameter, m
K	Hydraulic permittivity, m^2
K_s	Splashing parameter
L	Length, m
Nu	Average Nusselt number based on the hydraulic diameter
Oh	Ohnesorge number
∇p	Pressure drop, Pa/m
$\frac{dp}{dz}$	Linear pressure drop, Pa/m
Pr	Prandtl number
n_d	Droplet spread parameter
Y	Mass fraction
Re	Reynolds number
Re_p	Relative Reynolds number of a particle
Re_1	Modified Kozeny-Carman Reynolds number
Sc	Schmidt number
S_v	Specific surface area, m^2/m^3
t	Time, s
U_{GS}	Frontal superficial gas velocity, m/s
v_f	Fluid phase velocity normal to the cross-section displacement, m/s
We	Weber number

Abbreviations

CFD	Computational Fluid Dynamics
MRCV	Mean Representative Cubic Volume
RTD	Residence Time Distribution
SEM	Scanning Electron Microscopy

SiSiC	Silicon-infiltrated Silicion Carbide

Greek symbols

α	Permittivity constant related to the pore properties
β	Forchheimer constant related to the pore properties
ε	Porosity
μ_L	Liquid dynamic viscosity, Pa · s
μ_{mol}	Molecular viscosity, Pa · s
ρ_L	Liquid density, $\mathrm{Kg/m^3}$
σ_{lv}	Liquid-vapor surface tension, N/m

Subscripts

g	Gas
l	Liquid
d	Droplet

Supporting Information

Table S1. Parameters of the droplet RTDs in accordance with the modified Dagum distribution.

References

(1) Steimes, J.; Hendrick, P. Measurement and Prediction of Droplet Size in Annular Gas–Liquid Flows in Aero-Engine Oil Systems. *Int. J. Multiph. Flow* **2017**, *93*, 84.

(2) Wahba, E. M.; Nawar, H. Multiphase Flow Modeling and Optimization for Online Wash Systems of Gas Turbines. *Appl. Math. Model.* **2013**, *37*, 7549.

(3) Al-Dughaither, A. S.; Ibrahim, A. A.; Al-Masry, W. A. Investigating Droplet Separation Efficiency in Wire-Mesh Mist Eliminators in Bubble Column. *J. Saudi Chem. Soc.* **2010**, *14*, 331.

(4) Aliabadi, A. A.; Rogak, S. N.; Bartlett, K. H.; Green, S. I. Preventing Airborne Disease Transmission: Review of Methods for Ventilation Design in Health Care Facilities. *Adv. Prev. Med.* **2011**, *2011*, 124064.

(5) Edouard, D.; Lacroix, M.; Huu, C. P.; Luck, F. Pressure Drop Modeling on SOLID Foam: State-of-the Art Correlation. *Chem. Eng. J.* **2008**, *144*, 299.

(6) Nie, Z.; Lin, Y.; Tong, Q. Modeling Structures of Open Cell Foams. *Comput. Mater. Sci.* **2017**, *131*, 160.

(7) Zalucky, J.; Wagner, M.; Schubert, M.; Lange, R.; Hampel, U. Hydrodynamics of Descending Gas-Liquid Flows in Solid Foams: Liquid Holdup, Multiphase Pressure Drop and Radial Dispersion. *Chem. Eng. Sci.* **2017**, *168*, 480.

(8) Lacroix, M.; Nguyen, P.; Schweich, D.; Pham Huu, C.; Savin-Poncet, S.; Edouard, D. Pressure Drop Measurements and Modeling on SiC Foams. *Chem. Eng. Sci.* **2007**, *62*,

3259.

(9) Du Plessis, P.; Montillet, A.; Comiti, J.; Legrand, J. Pressure Drop Prediction for Flow through High Porosity Metallic Foams. *Chem. Eng. Sci.* **1994**, *49*, 3545.

(10) Diani, A.; Bodla, K. K.; Rossetto, L.; Garimella, S. V. Numerical Analysis of Air Flow through Metal Foams. *Energy Procedia* **2014**, *45*, 645.

(11) Simcik, M.; Ruzicka, M. C.; Mota, A.; Teixeira, J. A. Smart RTD for Multiphase Flow Systems. *Chem. Eng. Res. Des.* **2012**, *90*, 1739.

(12) Zou, Z.; Zhao, Y.; Zhao, H.; Zhang, L.; Xie, Z.; Li, H.; Zhu, Q. CFD Simulation of Solids Residence Time Distribution in a Multi-Compartment Fluidized Bed. *Chinese J. Chem. Eng.* **2017**, *25*, 1706.

(13) Kalaga, D.; Reddy, R.; B. Joshi, J.; V. Dalvi, S.; Nandakumar, K. Liquid Phase Axial Mixing in Solid–Liquid Circulating Multistage Fluidized Bed: CFD Modeling and RTD Measurements. *Chem. Eng. J.* **2012**, *191*, 475.

(14) Cruz-Díaz, M. R.; Rivero, E. P.; Almazán-Ruiz, F. J.; Torres-Mendoza, Á.; González, I. Design of a New FM01-LC Reactor in Parallel Plate Configuration Using Numerical Simulation and Experimental Validation with Residence Time Distribution (RTD). *Chem. Eng. Process. Process Intensif.* **2014**, *85*, 145.

(15) Rueden, C. T.; Schindelin, J.; Hiner, M. C.; DeZonia, B. E.; Walter, A. E.; Arena, E. T.; Eliceiri, K. W. ImageJ2: ImageJ for the next Generation of Scientific Image Data. *BMC Bioinformatics* **2017**, *18*, 529.

(16) Doube, M.; Kłosowski, M. M.; Arganda-Carreras, I.; Cordelières, F. P.; Dougherty, R. P.; Jackson, J. S.; Schmid, B.; Hutchinson, J. R.; Shefelbine, S. J. BoneJ: Free and Extensible Bone Image Analysis in ImageJ. *Bone* **2010**, *47*, 1076.

(17) Thiago Piazera de Carvalho. Two-Phase Flow in Open-Cell Metal Foams with Application to Aero-Engine Separators, University of Nottingham, 2016.

(18) ANSYS, I. ANSYS Fluent Theory Guide.

(19) Elghobashi, S. On Predicting Particle-Laden Turbulent Flows. *Appl. Sci. Res.* **1994**, *52*, 309.

(20) Armand, P.; Boulaud, D.; Pourprix, M.; Vendel, J. Two-Fluid Modeling of Aerosol Transport in Laminar and Turbulent Flows. *J. Aerosol Sci.* **1998**, *29*, 961.

(21) Morsi, S. A.; Alexander, A. J. An Investigation of Particle Trajectories in Two-Phase Flow Systems. *J. Fluid Mech.* **1972**, *55*, 193.

(22) Lecrivain, G.; Hampel, U. Influence of the Lagrangian Integral Time Scale Estimation in the Near Wall Region on Particle Deposition. *J. Fluids Eng.* **2012**, *134*, 1.

(23) D., S. C.; G., H. M.; Michael, Z. J. An Experimental Investigation of Fluid Flow Resulting from the Impact of a Water Drop with an Unyielding Dry Surface. *Proc. R. Soc. London. A. Math. Phys. Sci.* **1981**, *373*, 419.

(24) Mundo, C.; Sommerfeld, M.; Tropea, C. On the Modeling of Liquid Sprays Impinging on Surfaces. *At. Sprays* **1998**, *8*, 625.

(25) Rosa N., G.; Villedieu, P.; J, D.; Lavergne, G. *A New Droplet-Wall Interaction Model*;

2008.

(26) Roisman, I. V; Lembach, A.; Tropea, C. Drop Splashing Induced by Target Roughness and Porosity: The Size Plays No Role. *Adv. Colloid Interface Sci.* **2015**, *222*, 615.

(27) Latka, A.; Boelens, A. M. P.; Nagel, S. R.; de Pablo, J. J. Drop Splashing Is Independent of Substrate Wetting. *Phys. Fluids* **2018**, *30*, 22105.

(28) Almohammadi, H.; Amirfazli, A. Droplet Impact: Viscosity and Wettability Effects on Splashing. *J. Colloid Interface Sci.* **2019**, *553*, 22.

(29) A. Gipperich A. N. Lembach, I. V. R.; Tropea, C. On the Splashing Threshold of a Single Droplet Impacting onto Rough and Porous Surfaces. In *ILASS - Europe 2010, 23rd Annual Conference on Liquid Atomization and Spray Systems, Brno, Czech Republic*; 2010; p 1.

(30) O'Rourke, P. J.; Amsden, A. A. A Spray/Wall Interaction Submodel for the KIVA-3 Wall Film Model. *SAE Technical Paper*. SAE International January 2000.

(31) Mundo, C.; Sommerfeld, M.; Tropea, C. Droplet-Wall Collisions: Experimental Studies of the Deformation and Breakup Process. *Int. J. Multiph. Flow* **1995**, *21*, 151.

(32) Li, G.; Mukhopadhyay, A.; Cheng, C.-Y.; Dai, Y. Various Approaches to Compute Fluid Residence Time in Mixing Systems. In *ASME 2010 3rd Joint US-European Fluids Engineering Summer Meeting collocated with 8th International Conference on Nanochannels, Microchannels, and Minichannels*; American Society of Mechanical Engineers (ASME): Quebec, Canada, 2010; Vol. 1, p 295.

(33) Lorensen, W.; E. Cline, H. Marching Cubes: A High Resolution 3D Surface Construction Algorithm. *ACM SIGGRAPH Comput. Graph.* **1987**, *21*, 163.

(34) Cabiddu, D.; Attene, M. Large Mesh Simplification for Distributed Environments. *Comput. Graph.* **2015**, *51*.

(35) Freitag, L. A. On Combining Laplacian And Optimization-Based Mesh Smoothing Techniques. *Am. Soc. Mech. Eng. Appl. Mech. Div.* **1997**, *220*, 37.

(36) Hildebrand, T.; Rüegsegger, P. A New Method for the Model-Independent Assessment of Thickness in Three-Dimensional Images. *J. Microsc.* **1997**, *185*, 67.

(37) Dougherty, R.; Kunzelmann, K.-H. Computing Local Thickness of 3D Structures with ImageJ. *Microsc. Microanal.* **2007**, *13*, 1678.

(38) Dukhan, N.; Patel, P. Equivalent Particle Diameter and Length Scale for Pressure Drop in Porous Metals. *Exp. Therm. Fluid Sci.* **2008**, *32*, 1059.

(39) Basavaraj, R. C. and M. G. *Flow of Fluids Through Granular Beds and Packed Columns.*, 6th ed.; Basavaraj, R. C. and M. G., Ed.; Butterworth-Heinemann, 2019.

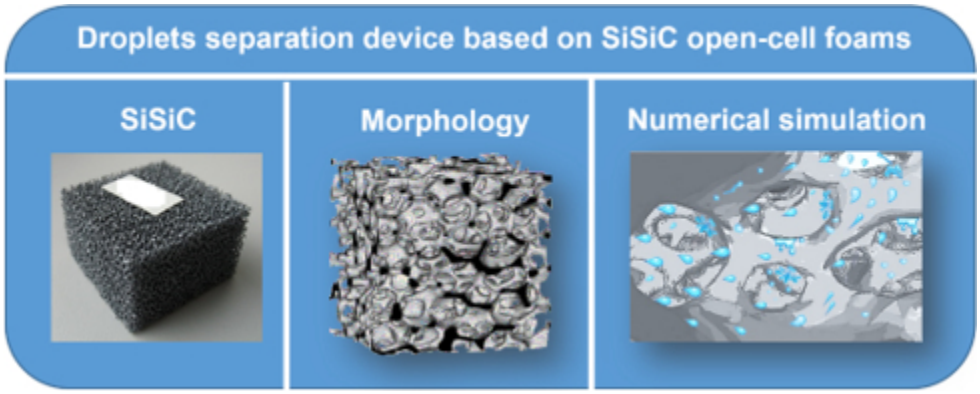

TOC

82x32mm (150 x 150 DPI)